5. Modulation Response

This chapter covers the modulation response of two-state quantum dot lasers, a quantity that can be easily measured and that is of crucial importance for communication applications [GRE13, LIN12, GIO11].

5.1. Data Transmission with Semiconductor Lasers

Semiconductor lasers are widely and commmonly used in optical data communication networks [GIO11, LIN12, GRE13], among other things as amplifiers [MEU09, SCH12e] or as mode-locked devices [ARS13]. As part of the ever expanding optical fiber networks, they are on the verge of becoming the backbone of modern information technology. Not only are all major parts of the long-distance connections, all submarine cables, no longer based on electronic transmission through copper lines, but optical fibers nowadays are also being used for internet access in private homes; in what the industry has termed 'fiber-to-the-home' connections [BON11].

Lasers based on self-assembled QDs possess a variety of advantages over other semiconductor systems and make them especially suited for these kinds of applications [BIM08]. They can emit at wavelengths of 1.3 μm and 1.5 μm, both of which are important as they represent minimum-loss cases for the currently installed optical fiber systems. With low threshold currents, high efficiency and long life times, QD lasers are among the most energy efficient lasers that are available. Additionally, temperature stability is very high caused by the discrete set of electronic states confined inside the QD box-like potential.

However, the most important factor is, of course, the maximum data transmission rate that can be achieved. In that regard QDs, at least in a Fabry-Perot-type device with no additional fabrication, do not reach as high of a modulation response as was theoretically predicted with simplified models in the 1980's [DIN76, ARA82, ASA86] as the finite time scattering processes limit the maximum carrier modulation that can be induced via varying the injection current [BIM08]. Current devices are able to reach error-free rates of up to 15 GHz [ARS14] as also theoretically described in [LIN12, LUE10a, LUE12].

Future improvements include vertical-cavity surface-emitting lasers, where a set of distributed Bragg-reflectors increases the reflectivity of the laser-cavity mirrors to above 99.9%. Here modulation rates of over 40 GBit/s [HOF11](Zitat) were achieved. Yet, out-coupling efficiencies and lasing intensities are low for such devices, as the high reflectivity leads to the concentration of lasing intensity only inside the active zone. Also actively being developed are electro-optical modulators, which offer a different approach. No longer relying on the carrier dynamics of the QD, the electriec field intensity is modulated directly, e.g. through voltage dependent absorption via the quantum-confined stark-effect, and even higher frequencies might be reached [WEG14].

Two-state lasing has so far not been in the focus of modulation-response related work. Only the modulation response of the ES has been compared to the GS [GIO06, VES07, ARS14], but no thorough current-dependent analysis has been published so far. This will be done by numerical simulation in the following sections.

A. Röhm, *Dynamic Scenarios in Two-State Quantum Dot Lasers,* BestMasters,
DOI 10.1007/978-3-658-09402-7_5, © Springer Fachmedien Wiesbaden 2015

5.2. Modelling of Modulation

When talking about modulation response, one has to make a distinction between a small-signal analysis and the larger modulation used for actually transmitting digital data. While the first is closely linked to perturbation induced relaxation oscillations and mimics a linear stability analysis, the latter includes more complex dynamics. In large signal analysis hysteretic effects can destroy the signal transmission at high frequency [LUE10a].

The small-signal modulation response of a QD device can be easily calculated with the numerical model. In experiments devices are fed a periodically modulated signal in the injection current. This can be included in the model by making the injection current J time dependent

$$J(t) = J^0 + \Delta J \sin(2\pi f t), \tag{5.1}$$

with a base current J^0, modulation amplitude ΔJ and modulation frequency f.

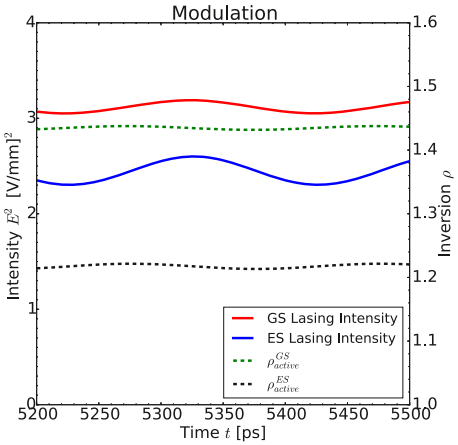

Figure 5.1: GS intensity (red) and active QD inversions $\rho^m_{act} = \rho^m_e + \rho^m_h$ for GS (green) and ES (blue) versus time. The injection current was modulated via $J(t) = J^0 + \Delta J \sin(2\pi f)$ and the resulting modulation of lasing field and carriers is shown for $2\pi f = 5$ GHz, $J^0 = 4 \times 10^{-5} e\text{nm}^{-2}\text{ps}^{-1}$ and $\Delta J = 0.5 \times 10^{-6} e\text{nm}^{-2}\text{ps}^{-1}$. This is a large modulation used to visualize the effect of a periodically varied injection current. Parameters as in table 4.

Figure 5.1 shows the resulting modulation of GS and ES electric field for $2\pi f = 0.5$ GHz, $J^0 = 4 \times 10^{-5} e\text{nm}^{-2}\text{ps}^{-1}$ and $\Delta J = 5 \times 10^{-6} e\text{nm}^{-2}\text{ps}^{-1}$. A periodic intensity fluctuation of the GS mode (red line) is achieved, while the relative fluctuation in carrier density is smaller. Even though the median ES intensity (blue line) is smaller, it is more strongly modulated by the injection current. This difference in the response is caused, in parts, by the faster capture channel for the ES carriers and the resulting stronger modulation of the ES inversion $\rho^{ES}_{act} = \rho^{ES}_e + \rho^{ES}_h$.

For visualization of this, Fig 5.2 shows the modulation response for identical parameters, but changed scattering rates. Here, the relaxation process S^{rel}_b was set to zero. To compensate for the loss of GS carrier input, GS capture $S^{GS,cap}_b$ was multiplied with a factor of 6. Detailed balance relations, however, were constantly

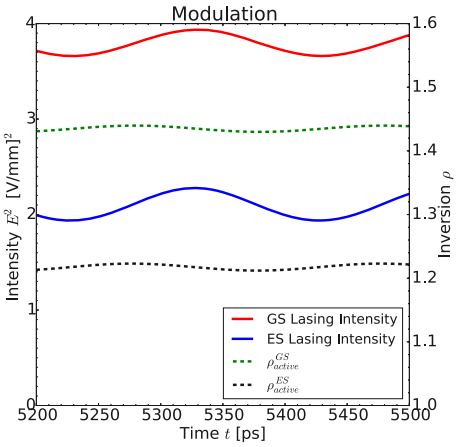

Figure 5.2: GS intensity (red) and active QD inversions $\rho^m_{act} = \rho^m_e + \rho^m_h$ for GS (green) and ES (blue) versus time for identical parameters as in Figure 5.1, but changed scattering rates. The relaxation scattering, meaning the direct exchange of carriers between ES and GS, was turned off and GS capture was speed up by a factor of six in this simulation. This illustrates the influence of the 'directness' of the carrier capture process on the resulting lasing intensity modulation. With GS capture now roughly twice as fast as ES capture, both resulting modulation amplitude are comparable in size.

maintained. As a result, the GS response is on the same order of magnitude as the ES response, illustrating that a direct, fast channel to the carrier reservoir is preferable to increase the amplitude of the modulated lasing intensity.

However, the fact that the GS capture has to be almost twice as fast as ES-capture also highlights that ES-amplitude is intrinsically stronger. While the scattering rates S determine how fast a given state equilibrates with the thermal distribution in the other carrier states, the equilibrium occupation ρ_{eq} itself also changes with injection current. As the Fermi distribution is less prone to perturbations for energies far from the Fermi-energy E_f, steady-state ES-carrier occupations have a stronger current-dependence. When the injection current is varied, this leads to higher carrier fluctuations than the GS, even if scattering time scales are the same.

The current-modulation amplitude ΔJ used here was rather large, to illustrate the effect of a sinusoidal signal on the injection current. In the following section, where frequency dependent amplitude responses will be calculated, a smaller ΔJ will be used, which is more in line with a small signal analysis.

5.3. Modulation Response Curves

The modulation response curve visualises the ability of the laser system to transfer a signal of the injection current into light intensity. As in the previous section the pump current was varied with $J(t) = J^0 + \Delta J \sin(2\pi f t)$, and the resulting intensity response $\Delta I^m = \Delta \|E^m\|^2$ with $m \in \{GS, ES\}$ is evaluated as a function of modulation frequency f. An example for parameters as in Tab. 4 and $J = 1 \times 10^{-5} e\text{nm}^{-2}\text{ps}^{-1}$ is shown in Fig. 5.3.

The modulation response is normalized with respect to the intensity response at low frequency ($f = 20$ MHz in this case). Which corresponds to the system relax-

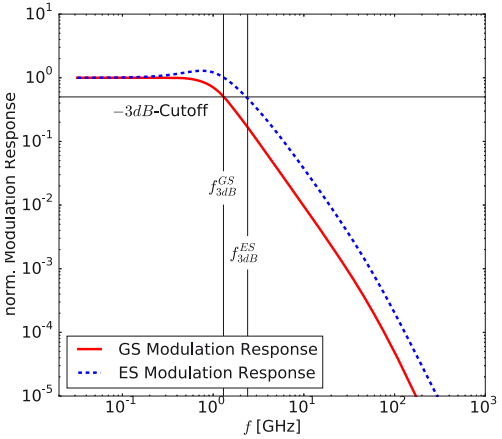

Figure 5.3: Normalised modulation response versus frequency f obtained by numerical simulation. The GS (red) and ES (blue) amplitude responses were normalized with respect to their low-frequency response. Where the relative strength of the light-intensity modulation drops below ~ 0.5 lies the 3dB-cut-off frequency f_{3dB}^{m}. Modulation responses can exhibit a resonance-feature, like the ES response in this picture, or simply diminish for high frequencies, like the GS here. Parameters as in Tab. 4, $J^0 = 1 \times 10^{-5} e\text{nm}^{-2}\text{ps}^{-1}$ and $\Delta J = 2 \times 10^{-7} e\text{nm}^{-2}\text{ps}^{-1}$.

ing to a steady state during each part of the modulation cycle; $I^m|_{J=J^0} - \Delta I^m = I^m|_{J=J^0-\Delta J}$. Contrarily, in the limit of very high frequencies ($f > 100GHz$ in Fig. 5.3) the system is far from reaching a steady state during one period of the modulation. Fluctuations are too fast for carrier populations to rise or fall. The system experiences only the median current J^0 and modulation is very weak. Therefore, the modulation strength is constant for the range of low frequencies and drops towards high frequencies.

For the right choice of parameters the lasing system can exhibit relaxation oscillations. These are tied to the eigenvalues of the system of differential equations. As the small-signal modulation disturbs the system only slightly, a linearisation of the system around the stable fix point for $J = J^0$ is a good approximation. Therefore, the damping and frequency of the relaxation oscillations are closely tied to the modulation response [LIN12].

In Fig. 5.3 this is visible for the ES in the shape of a resonance feature. For frequencies of about 1 GHz, the modulation response is exhibiting a maximum. By resonant excitation of relaxation oscillations the system's response is therefore greatly enhanced. Furthermore, this feature enhances the performance for faster modulation. The most important figure of merit in that regard is the '3dB-cut-off frequency' f_{3dB}^{m}. It is defined as the frequency where the relative strength of the light-modulation drops by 3 dB, which translates to a factor of $-3\text{dB} = 10^{-0.3} \simeq 0.5$. As a first estimate, this corresponds to the maximum frequency where almost error-free data transmission is still possible. Because the GS exhibits no relaxation oscillations and followingly lacks the resonance feature of the ES, the GS cut-off-frequency f_{3dB}^{GS} is lower than the ES cutoff f_{3dB}^{ES} (see Fig. 5.3, vertical lines).

Modulation response curves are often measured experimentally, as the amplitude of light intensity modulations can be easily obtained [GRE13, LIN12, GIO11]. They

are used in characterising a grown semiconductor laser sample and many publications, PhD theses and work groups are dealing with the right growth parameters for optimizing the laser performance, which usually means they try to reach as high values of the 3dB-cut-off frequency f_{3dB} as possible.

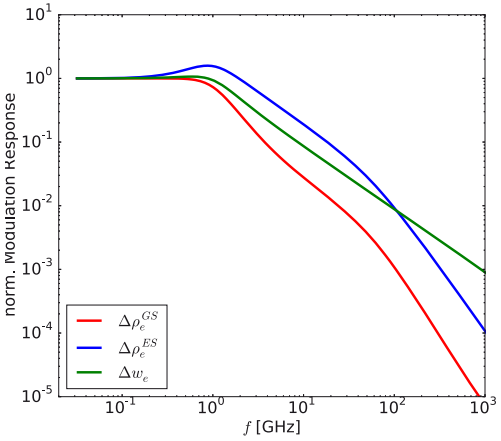

Figure 5.4: Normalised modulation response of w_e, ρ_e^{GS} and ρ_e^{ES} versus frequency obtained by numerical simulation. The excited state electrons (blue) exhibit a resonance feature, while both QW electrons and GS electrons exhibit none. Parameters as in Tab. 4, $J^0 = 1 \times 10^{-5} e\text{nm}^{-2}\text{ps}^{-1}$ and $\Delta J = 2 \times 10^{-7} e\text{nm}^{-2}\text{ps}^{-1}$.

For further study, Fig. 5.4 plots the normalised modulation response of QW electrons w_e, GS electrons ρ_e^{GS} and ES electrons ρ_e^{ES} versus frequency f. Defined analogously to intensity fluctuation, these carrier modulation responses are usually not readily available in experiments, but can be easily obtained in numerical simulations. The resonance feature of ES electrons matches the resonance of ES light intensity in Fig. 5.3. This is clear evidence of its relaxation-oscillation caused origin, as these oscillations stem from the periodic energy transfer between electron-hole pairs and photons. Furthermore, no resonance is visible for the two other electronic state occupations, which in turn do also exhibit strongly damped relaxation oscillations.

While the GS carrier dynamics are more complex, the shape of the w_e-modulation response is simply caused by the interplay of carrier-decay R^w_{loss} and the periodic injection current [LIN12], with the ES being additionally dominated by its resonance features. The analytic form for these response curves, which can be seen as an approximation of first order for all state variables, shall shortly be derived here.

Let $z \in \mathbb{C}$ denote a state variable and furthermore let its time evolution be described by three terms: First, a linear decay with time constant T; Second, an internal oscillation with frequency ω_{int}, e.g. modelling the periodic energy exchange with photons; Third, a time-dependant injection current $J(t) = J_0 + \Delta J \times e^{i\omega t}$ with external modulation frequency ω as a source. Thus, the differential equation for z is a driven harmonic oscillator:

$$\dot{z} = -\frac{z}{T} + i\omega_{int} z + J_0 + \Delta J \times e^{i\omega t}. \tag{5.2}$$

The steady state z_0 without modulation can then be derived via:

$$\begin{aligned} 0 =& -\frac{z_0}{T} + i\omega_{int} z_0 + J_0 \\ z_0 =& \frac{J_0 T}{1 - i\omega_{int} T} \end{aligned} \tag{5.3}$$

The time-dependant dynamics can be written as the steady state solution z_0 and a small time-dependant perturbation $\delta z(t)$. Inserting $z(t) = z_0 + \delta z(t)$ into Eq. (5.2) yields:

$$\begin{aligned} \dot{(z_0 + \delta z)} =& -\frac{z_0 + \delta z}{T} + i\omega_{int}(z_0 + \delta z) + J_0 + \Delta J e^{i\omega t} \\ \dot{z_0} + \delta\dot{z} =& -\frac{z_0}{T} + i\omega_{int} z_0 + J_0 - \frac{\delta z}{T} + i\omega_{int}\delta z + \Delta J e^{i\omega t} \\ \delta\dot{z} =& -\frac{\delta z}{T} + i\omega_{int}\delta z + \Delta J e^{i\omega t}. \end{aligned} \tag{5.4}$$

With the simple ansatz that z oscillates with the same frequency as the injection current, $\delta z = \Delta z e^{i\omega t}$, Eq. (5.4) becomes:

$$i\omega\Delta z e^{i\omega t} = -\frac{\Delta z}{T} e^{i\omega t} + i\omega_{int}\Delta z e^{i\omega t} + \Delta J e^{i\omega t}, \tag{5.5}$$

from which, after a short reshuffling, the complex modulation response $\Delta z/\Delta J$ can be extracted:

$$\frac{\Delta z}{\Delta J} = \frac{T}{1 + i(\omega - \omega_{int})T}, \tag{5.6}$$

and taking the absolute value yields:

$$\left|\frac{\Delta z}{\Delta J}\right| = \frac{T}{\sqrt{1 + (\omega - \omega_{int})^2 T^2}}, \tag{5.7}$$

which is the approximate shape for the modulation response curves. The drop-off towards high currents is furthermore given by:

$$\lim_{\omega \to +\infty} \left|\frac{\Delta z}{\Delta J}\right| = \frac{T}{\omega}, \tag{5.8}$$

which, in a double logarithmic plot, returns a straight line of slope -1.

Figure 5.5 shows w_e, ρ_e^{GS} and ρ_e^{ES} modulation response curves together with fits obtained via Eq. (5.7). The agreement for QW densities is good, which is also what can be expected as the reservoir carriers are directly modulated and their time

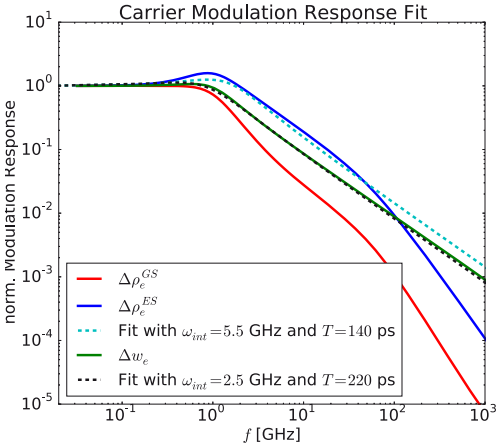

Figure 5.5: Normalised modulation response of w_e, ρ_e^{GS} and ρ_E^{ES} versus frequency obtained by numerical simulation, and analytical fits with Eq. (5.7). The fit for the directly modulated w_e-reservoir is shown by black dotted line, while the ES carriers' response is shown in light blue. No fit for the GS response could be obtained. Parameters for the numerical simulation as in Tab. 4, $J^0 = 1 \times 10^{-5} e\text{nm}^{-2}\text{ps}^{-1}$ and $\Delta J = 2 \times 10^{-7} e\text{nm}^{-2}\text{ps}^{-1}$; Fit parameters given in legend.

evolution most closely resembles the differential equation for z given in Eq. (5.2). However, the w_e decay rate of the numerical model in Eq. (2.68) is proportional to not only w_e, but also w_h. Which on a side note highlights, that the entirety of non-excitonic dynamics was not taken into account in the derivation of the fit of Eq. (5.7).

Despite this limitation, ES occupation-probability modulation $\Delta\rho_e^{ES}$ can be approximately reproduced with this fit. The resonance feature is weaker, yet overall agreement is good up to frequencies of $f \simeq 50$ GHz. At that point ES response is decaying even faster towards higher frequencies and is deviating from the previously predicted slope of -1 for high injection currents. As a result of previous works in the group of the author, it has been shown that this is linked towards the breakdown of carrier transport via scattering. Modulations do no longer propagate fast enough towards the confined QD states, but are kept within the QW-reservoir level. This can also be seen by the fact, that the w_e-response does not exhibit this scattering-related modulation break-down, as it is directly modulated via J.

Lastly, the ρ_h^{GS} modulation response of Fig. 5.5 was not reproduced. The dynamics here are clearly more complex than the simplistic approximations used for the fit. This is most probably related to the scattering dynamics, especially the strong dependence on ES occupations through the cascade scattering process QW-ES-GS. However, the modulation response drop-off at high frequencies can also be observed for the GS.

5.4. Cut-off-Frequencies and Two-State Lasing

After obtaining individual modulations and evaluating the response amplitudes, modulation response curves were introduced in the previous section. The 3dB-cut-off-frequency was introduced as the key figure of merit, often used in experiments to describe the maximum data transmission capacity of the device. Followingly, in this

section modulation response curves will be numerically calculated and their cut-off-frequencies be obtained as a function of pump current J, among other parameters.

Of special interest for this work is the interaction of modulation response with two-state lasing and GS quenching. The literature has not covered this topic extensively, and experimental verification of the predictions made here is therefore still lacking.

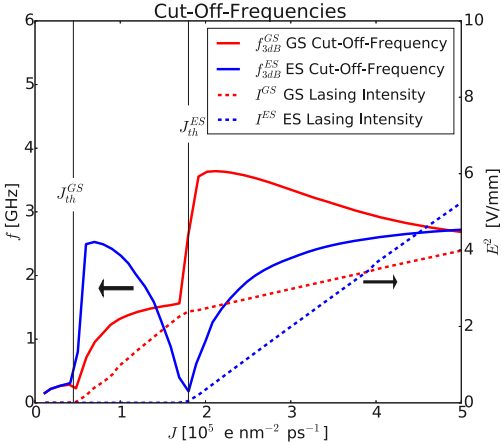

Figure 5.6: 3dB cut-off-frequencies for GS (red) and ES (blue) versus pump current obtained by numerical simulation. Light-current characteristic of the simulation shown in dashed lines. Parameters for the numerical simulation as in Tab. 4, $\Delta J = 2 \times 10^{-7} e\text{nm}^{-2}\text{ps}^{-1}$ and nonlinear scattering rates as in App. A.1.

Figure 5.6 shows the 3dB cut-off-frequencies for GS f_{3dB}^{GS} and ES f_{3dB}^{ES} as a function of pump current J. Also plotted as a reference is the light-current characteristic with dashed lines. There is clearly a connection between lasing thresholds and modulation response, as cut-off-frequencies obviously react when approaching lasing states. The individual details will be discussed in the following paragraphs.

The sub-threshold ES (blue solid line) cut-off-frequency reaches relatively high values with $f_{3dB}^{ES} > 2$GHz, yet as the ES is not lasing at this injection current, this is not useful for data transmission. As the ES lasing threshold is approached, modulation response is slowed down and reaches a minimum at $J = J_{th}^{ES}$. This can be partly tied to the relaxation oscillations slowing down at the threshold and partly attributed to the long effective carrier lifetime at threshold. The cut-off-frequency increases for injection currents and then saturates in agreement with previous works of QDs with only one confined state [GIO11, LUE12].

The GS dynamics in Fig. 5.6 exhibit a similar shape. Below GS threshold, GS modulation response is slow, reaches a minimum for $J = J_{th}^{GS}$ and increases nonlinear afterwards. However, the most striking feature is an almost vertical increase in the cut-off-frequency by a factor of two, when two-state lasing starts at $J = J_{th}^{ES}$. This is a phenomenon for which experimental verification is not available as of yet. Hence, from here on 'GS-modulation enhancement' will denote this sudden increase in the cut-off-frequencies for GS f_{3dB}^{GS} at the ES threshold. For high currents, the GS-modulation enhancement diminishes again and the GS cut-off-frequency approaches a static value (see also Fig. 5.12 for high-current behaviour).

5.5. Ground State Modulation Enhancement

Investigating this ES-lasing-induced GS-modulation enhancement is not finished and further research is necessary. Investigations are made difficult by the fact, that relaxation oscillations are almost nowhere present in the parameter ranges studied so far, as is generally the case for QD-based devices [BIM08a]. Numerically evaluating their damping and frequency, however, could have given a first clue towards the nature of this modulation enhancement. A drastic increase of GS relaxation oscillation frequency at the ES threshold current could explain the abrupt enhancement of the 3dB-cut-off-frequency.

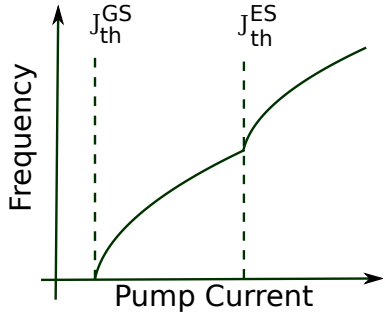

Figure 5.7: Relaxation oscillation frequency versus pump current as calculated by Abuusa *et al.* in [ABU13], schematically redrawn here. The drastic increase in the frequency coincides with the start of two-state lasing. Only a common frequency for both ES and GS was calculated.

However, an analytical approximation for the frequency of relaxation oscillations in two-state lasing lasers was published by Abuusa *et al.* in 2013 [ABU13]. They predict an increase of relaxation oscillation frequency for currents above the ES lasing threshold. The relevant figure from their work is schmetically redrawn here in Fig. 5.7.

However, it is questionable whether their analytical derivation is valid for the QDs simulated for this thesis. They only calculated a common relaxation oscillation frequency for both GS and ES, as they found no dynamical difference between both modes. This is in clear contrast with the rich dynamics seen in Fig 5.6, where GS and ES are clearly reacting differently. This could be caused by Abuusa *et al.* investigating mainly 'free' relaxation oscillations, which appear during turn-on, while the modulation response is 'driven' by an external source. Furthermore, their frequency always increases with current. Yet, the GS-modulation enhancement seen in Fig 5.6 seems to vanish for high currents, where cut-off-frequencies saturate. This suggests that the relaxation oscillation damping factor is at least as important as the frequency itself, as damping would have to increase strongly to suppress resonances.

A closer look to the injection current region of Fig. 5.6 in question also reveals that the resonance frequency does not shift. This can be seen in Fig. 5.8, where the absolute modulation response is shown for GS (red) and ES (blue) versus frequency. For the panel on the left the device was simulated at a current slightly below ES threshold $J < J_{th}^{ES}$, so the GS is lasing, while the ES is not. Correspondingly, ES absolute modulation response is weak in comparison to GS response, as ES intensity is purely caused by spontaneous emission (cf. the light-current characteristic in

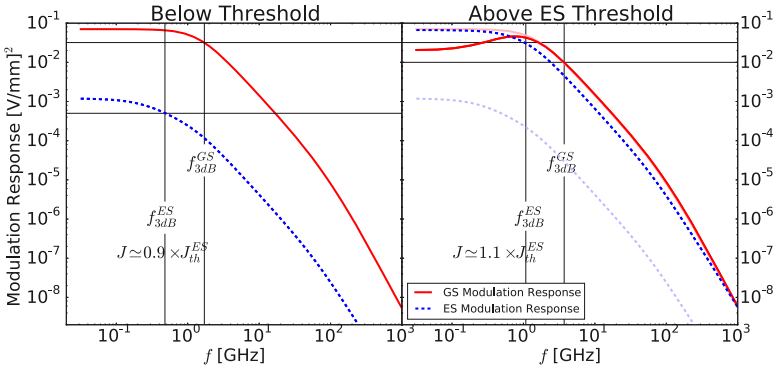

Figure 5.8: Absolute modulation response (not normalised) versus frequency f obtained by numerical simulation. ES (blue) and GS(red) modulation response is plotted on the same scale for currents $J < J_{th}^{ES}$ (left) and $J > J_{th}^{ES}$ (right.) Parameters for the numerical simulation as in Tab. 4, $\Delta J = 2 \times 10^{-7} e\text{nm}^{-2}\text{ps}^{-1}$ and nonlinear scattering rates as in App. A.1.

Fig. 5.6). Both response curves exhibit no clear maximum, and ES cut-off frequency is relatively low at $f_{3dB}^{ES} < 1$ GHz.

Figure 5.8 (right) shows the absolute modulation responses, in exactly the same scaling as on the left, for a current slightly above ES lasing threshold $J \simeq 1.1 J_{th}^{ES}$. With the ES intensity being greatly enhanced by stimulated emission, absolute modulation is similarly strengthened. Contrary to this, the high frequency flank of the GS modulation response is almost left unchanged. For frequencies around $f = 1$ GHz a resonance peak can be seen. This feature is 'revealed' by the receding low-frequency side of the GS modulation response curve. There, the absolute GS modulation is slightly weaker as compared to the lower injection currents in Fig. 5.8 (a), despite the fact that GS lasing intensity has risen. This is most pronounced for the flat part of the modulation response curve towards low frequencies $f < 0.1$ GHz.

This is also the reason, why no normalisation was used for Fig. 5.8. The low-frequency modulation response is always used as the baseline when normalising. This would result in a 'lifting' of the response curve, and the resonance feature appears to 'grow' out of the modulation response curve, as opposed to the low-frequency side receding and the resonance feature being left standing. Due to this renormalisation the cut-off-frequency for the GS f_{3dB}^{GS} is so greatly enhanced in Fig 5.6: The cut-off frequency is defined as the modulation frequency for which response intensity has dropped to $\simeq 0.5$ compared to the *low-frequency modulation response*, so when only the low-frequency modulation response is reduced, the cut-off frequency shifts to higher values.

Interpreting the observations told in the previous paragraphs, however, is not straight-forward. It seems that ES lasing is suppressing the low-frequency modulations in the GS; possibly by preventing carrier differences to propagate through the relaxation scattering channel. However, fast modulations are able to reach GS levels

regardless of the ES lasing state. Further investigations will therefore be presented.

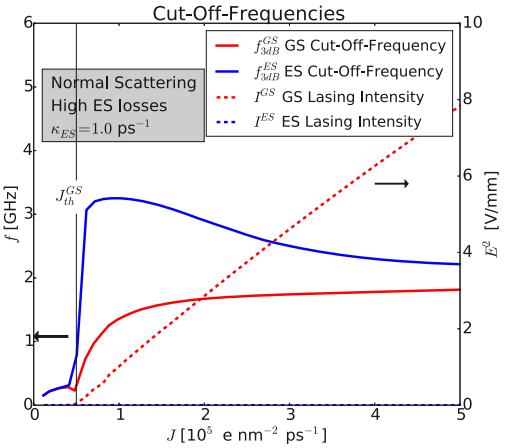

Figure 5.9: 3dB cut-off-frequencies for GS (red) and ES (blue) versus pump current obtained by numerical simulation. ES optical losses κ_{ES} were increased to prevent the ES from lasing. Consistently, Light-current characteristic of the simulation shown in dashed lines. Parameters for the numerical simulation as in Tab. 4, $\Delta J = 2 \times 10^{-7} e\text{nm}^{-2}\text{ps}^{-1}$, $\kappa_{ES} = 1.0\text{ps}^{-1}$ and nonlinear scattering rates as in App. A.1.

To verify, that it is really the onset of ES lasing that triggers this GS-modulation enhancement, Fig. 5.9 shows the GS and ES cut-off-frequencies and light-current characteristics with high optical losses in the ES. By setting $\kappa_{ES} = 1.0\text{ps}^{-1}$, the ES was prevented from achieving a lasing state. As a result no sudden GS-modulation enhancement is visible after the onset of GS lasing, so it is clear that ES photons must play an important role in the GS-modulation enhancement.

On a side note, the sudden increase of ES modulation at GS threshold, already seen in the first figure of cut-off-frequencies Fig. 5.6, is still visible. But with no ES lasing threshold present, there is no minimum in the ES cut-off-frequency, as was seen for $J = J^{ES}_{th}$ in Fig. 5.6, just a decline towards higher frequencies. So there certainly seems to be also a modulation enhancement in reverse direction, albeit the ES is not lasing at that point.

For further investigation, Fig. 5.10 shows the 3dB cut-off-frequencies for GS (red) and ES (blue) versus pump current, similar to Fig. 5.6. Here, however, GS capture rates were turned off, $S^{GS,cap}_{b,in/out} = 0$. Therefore, with any direct interaction between GS and QW prevented, any modulation reaching the GS must have been transmitted through the cascade scattering chain QW-ES-GS, and therefore ultimately through the ES as an intermediate reservoir.

The similarities between Fig. 5.10 and Fig. 5.6, however, suggest that direct GS capture processes play no major role. The sudden enhancement of the GS modulation response at the onset of ES lasing is still present. Furthermore, the fact that almost nothing else changes can be attributed to the nature of the microscopically calculated scattering rates, i.e. the resulting GS capture rates are always slower than the cascade-scattering channel consisting of ES capture and relaxation.

Now, the opposite approach is shown in Fig. 5.11, where the relaxation scattering was turned off, $S^{rel} = 0$. This leads to a decoupling of the GS and ES and they

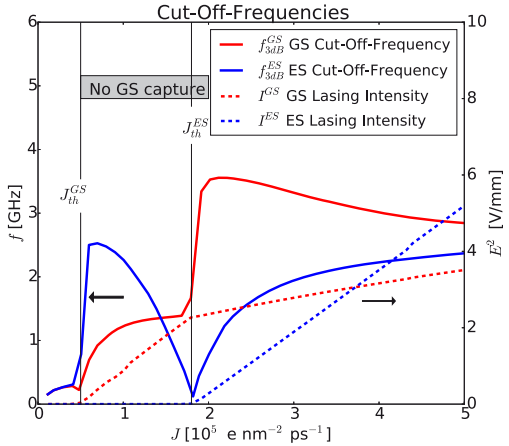

Figure 5.10: 3dB cut-off-frequencies for GS (red) and ES (blue) versus pump current obtained by numerical simulation. As opposed to Fig. 5.6, direct scattering from GS to QW were turned off. Light-current characteristic of the simulation shown in dashed lines. Parameters for the numerical simulation as in Tab. 4, $\Delta J = 2 \times 10^{-7} e\text{nm}^{-2}\text{ps}^{-1}$ and linearised scattering rates as in App. A.2, with $S^{GS,cap}_{b,in/out} = 0$.

only indirectly interact through the reservoir carrier densities w_b. The strong GS-modulation enhancement feature is not present in this simulation. The overall shape of the cut-off-frequency curve is in agreement with simulations of QDs including only a single confined state [GIO11, LUE12].

Yet, there still remains some cross-influence between GS and ES. The ES cut-off frequency is clearly enhanced once the GS lasing threshold is crossed $J^{GS}_{th} < J < J^{ES}_{th}$, just like in the previous simulations of Fig. 5.6, 5.9 and 5.10. Furthermore, there seems to be a drastic enhancement of GS modulation, for a current in between GS and ES thresholds. This is, however, not the feature linked to the appearance of the ES. The individual modulation response curves (not shown here) look clearly different to Fig. 5.8.

To conclude this section, the anomalous GS cut-off-frequency increase was investigated. It has been shown to be linked to the onset of ES lasing and dependent on the relaxation scattering process, while it is not dependent on the direct capture from the QW. To the contrary, turning off the relaxation leads to the disappearance of this modulation enhancement.

From modulation response curves below and above ES thresholds, one can deduce that the ES acts like a high-pass filter, blocking only the low-frequency modulations from reaching the GS. This leads to the appearance of a resonance feature, enhancing the cut-off-frequency. It therefore seems that ES photons are acting as a buffer that reduce the modulation propagated to the GS.

5.6. Change of Cut-Off-Frequency with Carrier Loss Rates

Apart from the ES-lasing induced GS modulation enhancement studied in the previous section, there are other ways of increasing the maximum data transmission rate of QD-based devices. Two of these will shortly be covered in this section.

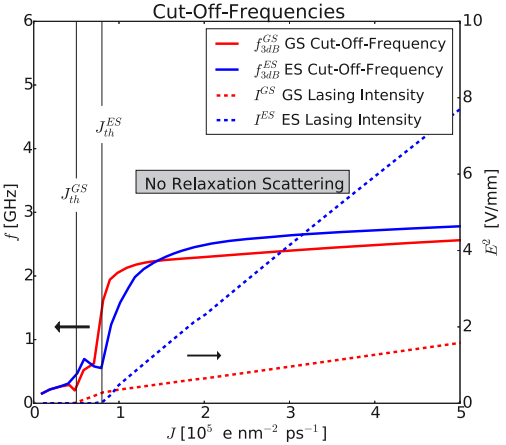

Figure 5.11: 3dB cut-off-frequencies for GS (red) and ES (blue) versus pump current obtained by numerical simulation. Light-current characteristic of the simulation shown in dashed lines. Relaxation from ES to GS was turned off, so that both carrier states are directly fed from the well. Parameters for the numerical simulation as in table 4, $\Delta J = 2 \times 10^{-7} e\text{nm}^{-2}\text{ps}^{-1}$ and linearised scattering rates as in App. A.2, with $S^{rel} = 0$.

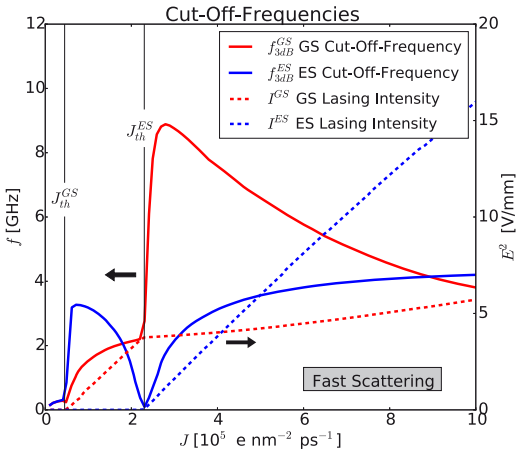

Figure 5.12: 3dB cut-off-frequencies for GS (red) and ES (blue) versus pump current obtained by numerical simulation. Light-current characteristic of the simulation shown in dashed lines. Scattering rates were speed up by a factor of three, resulting in an increase of the cut-off-frequencies. Note the different scaling compared to previous figures, showing high-current dynamics where cut-off frequencies approach a constant value. Parameters for the numerical simulation as in Tab. 4, $\Delta J = 2 \times 10^{-7} e\text{nm}^{-2}\text{ps}^{-1}$ and nonlinear scattering rates as in App. A.1, multiplied with a factor of 3.

The most straight-forward way when simulating is by simply increasing the scattering rates. Fig. 5.12 shows the 3dB cut-off-frequencies for GS (red) and ES (blue) versus pump current obtained by numerical simulation for all scattering rates three times as fast. Note the different axis scaling compared to Fig. 5.6. The modulation response is faster, while all features are maintained. Also shown is the high-current range, for which both ES and GS cut-off-frequencies approach a constant value.

However, scattering rates cannot be simply increased in experiments, where they depend on QD shape, device structuring and material [BIM08], all of which have to already be controlled to yield correct telecommunication wavelengths and leave little room for further adjustments.

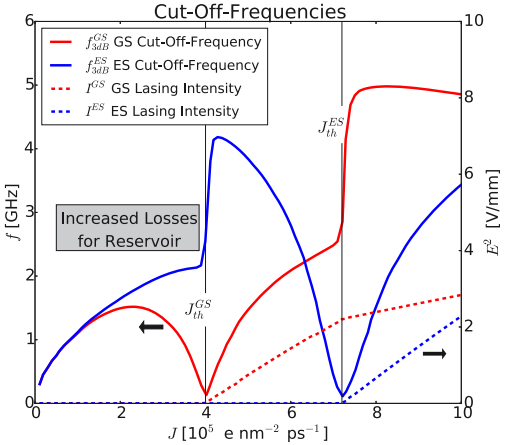

Figure 5.13: 3dB cut-off-frequencies for GS (red) and ES (blue) versus pump current obtained by numerical simulation. Light-current characteristic of the simulation shown in dashed lines. . Parameters for the numerical simulation as in Tab. 4, $\Delta J = 2 \times 10^{-7} e\text{nm}^{-2}\text{ps}^{-1}$, $R_{loss}^{w} = 0.59\text{nm}^2\text{ps}^{-1}$ and nonlinear scattering rates as in App. A.1.

The interplay of carrier lifetime, mostly given by the combined loss term R_{loss}^{w} in the numerical model, with modulation response is complex [LIN12]. However, in the parameter range of this thesis, an increase of losses is predicted by Lingnau et al. to yield higher cut-off-frequencies. The results of a simulation with $R_{loss}^{w} = 0.59\text{nm}^2\text{ps}^{-1}$ is shown in Fig. 5.13. In accordance with the prediction, cut-off-frequencies are increased by $\sim 25\%$ in the GS and $\sim 40\%$ in the ES. However, this comes at the cost of higher threshold injection currents for both GS and ES.

5.7. Outlook for Modulation Response

To end this chapter, a last simulation shall be presented, highlighting the need for further work in this area. Figure 5.14 shows the cut-off-frequencies for GS and ES. Here, scattering rates were changed to lead to hole depletion and subsequent GS quenching by reducing hole capture rates to 5% as has been done in Sec. 4.2. The resulting cut-off-frequencies display rich dynamics. The individual modulation response curves for all currents were individually checked, to assure that no numerical error caused this behaviour.

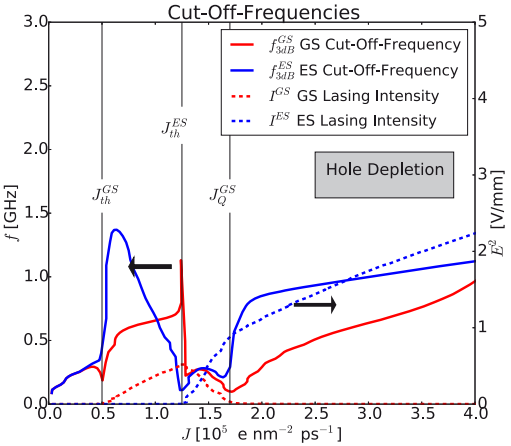

Figure 5.14: 3dB cut-off-frequencies for GS (red) and ES (blue) versus pump current obtained by numerical simulation. Scattering rates were changed to yield hole-depletion induced GS quenching. Light-current characteristic of the simulation shown in dashed lines. Parameters for the numerical simulation as in Tab. 4, $\Delta J = 2 \times 10^{-7} e\text{nm}^{-2}\text{ps}^{-1}$ and linearised scattering rates as in App. A.2, hole captures reduced to 5%.

For one, the GS modulation cut-off frequency is *not* increased once two-state lasing starts, but apart from a small peak decreased. Additionally, overall performance has been greatly degraded with cut-off-frequencies well below 2GHz for most of the current range. However, the turned-off GS displays strong increase in the cut-off frequency for currents well above the GS quenching thresholds ($f \simeq 4.5$GHz), not seen in any other simulation so far. However, the GS is already turned off at that point.

Understanding all of these features, linking them to real and artificial causes of the parameters chosen, and examining the ones useful for data transmission is a topic suited for future research. In addition to pure numerical simulation of modulation response curves for even other scattering and parameter sets, there are several other points of interest.

The ES-lasing-induced GS modulation enhancement needs a verification of its suitability for data transmission. As seen form the individual modulation response curves, it is a suppression of low-frequency response that increases the 3dB cut-off-frequency. The high-frequency flank, however, stays almost constant when measured in absolute terms. This begs the question, whether a large signal analysis would actually yield decodable bits and needs to be studied.

Second, apart from the purely numerical study done here, a deeper, more physical understanding of the phenomenon needs to be developed. A good beginning could be deriving an analytical approximation. One might approximate the system as coupled, damped harmonic oscillators, of which only one is driven. Furthermore, the low-frequency range can probably be studied with steady-state simulations.

Lastly, the non-monotonous shape of cut-off-frequencies might be useful in designing experiments. As it appears that the GS modulation enhancement with ES lasing is linked to the relaxation scattering channel, it might be used to determine the strength of this scattering process in real QDs. Furthermore, if the cut-off frequency

shape shown here for hole-depletion induced GS quenching can be generalised for a broad variety of parameters, measurements of the modulation responses could also be used to unambiguously determine the cause of GS quenching experimentally.